NUMERICAL SIMULATION OF PARTICLE TRANSPORT IN PLANAR SHEAR LAYERS

S. K. AGGARWAL[1], J. B. YAPO[1], F. F. GRINSTEIN[2] and K. KAILASANATH[2]

[1]Department of Mechanical Engineering, University of Illinois at Chicago, Chicago, IL 60680, U.S.A.
[2]Laboratory for Computational Physics and Fluid Dynamics, Naval Research Laboratory, Washington, DC 20375, U.S.A.

Abstract—Numerical simulations of particle dispersion in a planar shear dominated by large scale vortical structures are reported. The shear layer is formed by two co-flowing streams past a splitter plate. The emphasis of this work is on examining how the particle dynamics are affected by the large-scale coherent structures in the initial development of the instabilities in a spatially-developing mixing layer. The two-dimensional time-dependent gas-phase equations are solved numerically using the explicit flux corrected transport (FCT) algorithm in the low-Mach-number regime. The dispersion of particles is studied by following their trajectories in the shear layer. A detailed visualization of the flow field, dominated by the large structures, and of the particle dynamics is performed to obtain qualitative as well as quantitative information on the particle dispersion. The visualization clearly reveals the capturing of the small and intermediate size particles by the vortical structures. The small size particles, however, remain captured in the vortical structures, whereas the intermediate size particles are flung out of them, leading to their enhanced dispersion. The large particles remain mostly unaffected by the large eddies. The quantitative results obtained indicate that the above behavior can be well correlated with the Stokes number (S_t) values; the optimal dispersion corresponds to the Stokes numbers in the range $0.1 < S_t < 5.0$. This is in qualitative agreement with previously reported experimental as well as numerical results. The results also indicate that the particles injected in the faster stream exhibit higher dispersion compared to those injected in the slower stream. This divergence in the dispersion behavior is related to the asymmetric entrainment as reported by some earlier experimental and numerical studies.

INTRODUCTION

Particle-laden turbulent flows occur in numerous technological applications. These include many propulsion and energy conversion systems such as gas turbines, rocket engines and boilers, as well as industrial systems such as coating, painting and spray cooling devices. There are also many physiological and environmental situations involving two-phase turbulent flows.

The traditional approaches for describing these flows have been based on obtaining the average behavior of the turbulent carrier fluid by using the time- or Favre-averaged governing equations along with some semi-empirical turbulence models. The dispersed phase is represented by a large number of discrete particles and their dynamic behavior is determined in a deterministic manner. The coupling between the phases is provided by the interaction terms, representing the exchange of mass, momentum and energy. These terms are continuously updated during the computation. The effect of turbulence on the particle trajectories or the dispersion effect is modeled either by imparting a diffusional velocity to the particles [1, 2] or by using a stochastic approach [3, 4] to obtain a fluctuating gas (carrier fluid) velocity field that is added to the mean gas velocity field. In the latter approach, which is more commonly used, the turbulent (fluctuating) gas velocity is determined by assuming that the turbulence is isotropic with a Gaussian distribution and the variance is given by $2k/3$ where k is the turbulent kinetic energy. The variance is multiplied by a random number to yield the fluctuating velocity component.

A number of experimental and computational studies [5–11], published during the last two decades, have shown that the turbulent flows, which previously were thought to be totally chaotic and statistical in nature, are dominated by large-scale coherent vortical structures. This has caused a major shift in thinking as to how the dynamics of turbulence be perceived and modeled. In fact, a number of important questions have been posed by these studies. How useful or relevant are the semi-empirical models based on the Reynolds or Favre-averaged approach? How strongly are the

mixing and entrainment processes influenced by the generation and evolution of the organized structures? How does the dynamic interaction of large-scale and small-scale structures (molecular mixing) determine the processes of chemical reaction, ignition, flame stability and extinction? How is particle dispersion behavior affected by the large-scale structures and in turn how are these structures influenced by the dispersed phase? Although the results reported in Refs [5–11] and others have not provided satisfactory answers to these questions, they have seriously challenged the adequacy of the traditional approaches for accurately describing the turbulent two-phase flows.

In this paper, the numerical simulations of particle dynamics and dispersion in a planar shear layer are reported. The shear layer formed downstream of a splitter plate is simulated by solving the time-dependent inviscid compressible conservation equations using the explicit Flux Corrected Transport (FCT) algorithm [12, 13]. The numerical model is first used to predict the evolution of the Kelvin–Helmholtz instability, including the formation and subsequent merging of large-scale vortices in the early development of the instabilities in the mixing layer. Then, at a specified time which is a parameter in the study, the particles of given size and velocity are injected continuously from the specified locations in the cross stream direction. The dynamics and dispersion of these particles as influenced by the large scale structures are studied by solving the particle equations based on the Lagrangian approach. Numerical results are presented to highlight the particle dispersion caused by the coherent vortical structures. The results also indicate the selective nature of the dispersion process. Not only does the dispersion function depend on the particle size, it is also a function of the initial injection location in the cross-stream direction, which underscores the asymmetric nature of the mixing process, as well as of the time of injection. In addition, it is shown that the dispersion function does not decrease monotonically as the particle size is increased. The last result substantiates the findings of previous studies reviewed by Crowe *et al.* [10] and of more recent experimental work reported by Lazaro and Lasheras [14, 15].

Previous works on mixing layer simulations have employed spectral [16, 17], vortex dynamics [18] and finite-difference [9, 13, 19, 20] techniques. These studies have focused on the dynamics of large-scale structures either in temporally developing mixing layer [16, 17] or in spatially developing layers [18–20]. The former approach is computationally more efficient because of the relatively compact spatial domain. However, the spatially developing case resembles more closely to the laboratory as well as practical situations. Notable experimental studies pertinent to the present paper are due to Lazaro and Lasheras [11, 14, 15], and Hishida *et al.* [21]. Hishida *et al.* [21] investigated the dispersion of solid particles in a planar shear layer and observed a strong correlation between the particle dispersion and the Stokes number, defined as the ratio of the particle response time to the characteristic time of the large-scale eddies. For a range of Stokes number between 0.5 and 2.5, the particles were observed to disperse more significantly than the gas phase. Lazaro and Lasheras [14, 15] conducted a comprehensive experimental study of particle dispersion in unforced and forced planar mixing layers. For the unforced case, they used flow visualization and spectral analysis, and observed the central role played by the large-scale turbulent motion in the particle dispersion process. Unlike in the unforced shear layer, the particle dispersion
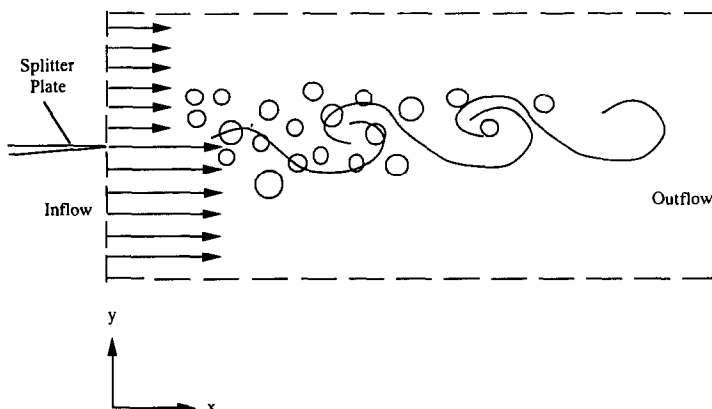

Fig. 1. Schematic of the physical model and computational domain.

in the forced shear layer was shown to be a size-selective process characterized by the existence of an intermediate particle size range for which the lateral dispersion is maximized. The simulations presented in this paper also exhibit an intermediate droplet size range for the maximum lateral dispersion. A further comparison is provided later in the paper. Previous numerical studies [10, 22, 23] on the particle dynamics in turbulent mixing layers employing the discrete vortex approach have also been reported. The present work differs from those studies in the numerical approach employed. An important consequence of this difference is the asymmetric dispersion behavior which is not captured in the previous studies. There are other important differences as discussed later. In addition, a more general approach is followed in the present investigation such that other important phenomena such as the effect of forcing and vaporization on droplet dispersion as well as the effect of droplets on the dynamics of large-scale structures can be studied.

The organization of the paper follows a standard format. The physical model and the governing equations are described next. This is followed by the discussion of the results. The conclusions are presented in the last section.

THE PHYSICAL AND NUMERICAL MODEL

A splitter-plate flow configuration is considered in the present study. Two coflowing parallel streams with a velocity difference are considered at the trailing edge of a splitter plate. A schematic of the physical model and the computational domain marked by the broken line are shown in Fig. 1. The computational grid is given in Fig. 2. As indicated, a variable grid size is employed so as to locate more points in the initial region ($0 < x < 3.6$ cm) near the centerline where the instability first occurs and the coherent structures form. Due to the pairing and merging process, the spanwise vortical structures grow in size as they convect downstream. The grid size in x direction is continuously stretched downstream such that larger computational cells can be used to resolve the larger structures. In a similar way, the grid size in y direction is stretched further away from the centerline.

The droplets of given size and velocity are injected at the specified locations in the cross-stream direction at the inflow boundary ($x = 0$). The instant when the droplet injection is first initiated and the period between two consecutive injections are considered as parameters in the study. The time-dependent governing equations for the conservation of gas-phase mass, momentum, and energy are:

$$\frac{\partial \rho}{\partial t} = -\nabla \cdot \rho V + S_\rho \tag{1}$$

$$\frac{\partial}{\partial t}(\rho V) = -\nabla p - \nabla \rho \cdot VV + S_v \tag{2}$$

$$\frac{\partial E}{\partial t} = -\nabla \cdot VE - \nabla \cdot pV + S_e \tag{3}$$

where

$$E = e + \frac{1}{2}\rho\left(V_x^2 + V_y^2\right) \tag{4}$$
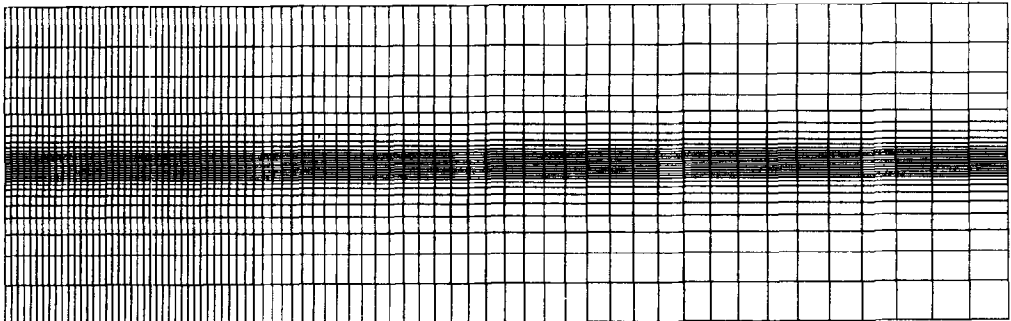

Fig. 2. Variable grid system.

and

$$e = \frac{p}{\gamma - 1}.$$ (5)

In the above equation, ρ is the density, p the pressure, e the internal energy, V the velocity vector, and γ the ratio of specific heats. The terms S_ρ, S_v, and S_e represent, respectively, the source/sink terms due to the exchange of mass, momentum and energy with the dispersed phase. In the present study, these terms are negligible since only a few thousand particles with diameters less than 100 microns are considered. In other words, an ultra-dilute two-phase flow is being simulated with only a one-way coupling, i.e. the particles are influenced by the gas phase and not vice versa. The dynamic equations governing the trajectory and velocity of a particle can be written as

$$\frac{dX_p}{dt} = V_p$$ (6)

$$\frac{4}{3} \pi r_p^3 \rho_p \frac{dV_p}{dt} = F$$ (7)

where X_p and V_p are, respectively, the position and velocity vectors for a particle represented by the subscript p, ρ_p is the material density of the dispersed phase, and r_p is the particle radius. The force F in equation (7) is assumed to be due to the drag force on the particle. This implies that the contribution of the flow non-uniformities, flow acceleration, and Basset history terms [24] to F are assumed to be negligible in comparison with the drag term. This is, however, not a limitation of the present study. Moreover, as discussed by Faeth [25], these terms can be neglected when $\rho_p/\rho \sim 10^3$. For the results presented here, $\rho_p = 1.0$ g/cm^3 whereas the initial gas density is assumed to be 1.182×10^{-3} g/cm^3. F is given by

$$F = C_d \frac{1}{2} \pi r_p^2 \rho \, |V - V_p|(V - V_p)$$ (8)

where the drag coefficient C_d is assumed to be given by the solid sphere drag correlation [22] as

$$C_d = \frac{24}{Re_p}\left(1 + \frac{Re_p^{2/3}}{6}\right)$$ (9)

and

$$Re_p = \frac{2\rho \, |V - V_p| r_p}{\mu}$$ (10)

where μ is the gas viscosity.

Boundary conditions

The free slip boundary conditions are specified at the top and the bottom boundaries of the computational domain. At the left boundary, the inflow density and velocity are specified, and the pressure is allowed to float by employing a zero-gradient condition. As discussed by Grinstein et al. [26], this allows the pressure at the inflow to adjust to the disturbances arriving from downstream and the feedback mechanism to retrigger the instability. The importance of feedback in subsonic shear flows in the laboratory has been noted earlier [7]. A step function as well as hyperbolic-tangent velocity profiles were used at the inflow boundary. The development and subsequent evolution of large-scale structures were found to be qualitatively insensitive to these velocity profiles. One such result showing the effect of initial velocity profiles on particle dispersion is discussed later in the paper.

A subsonic flow simulation requires a special treatment of the boundary conditions at an outflow boundary. Zeroth order-extrapolations are employed for the density and velocities. The pressure at the guard cell, which is one grid length downstream of the last computational cell, is calculated by using

$$p_g = p_n + (X_g - X_n)(p_{amb} - p_n)/(X_g - X_o)$$ (11)

where the subscripts g and n refer, respectively, to the guard cell and the last cell in the computational domain. X is the location of the inflow boundary and p_{amb} is the pressure far away from the outflow boundary. The above equation is obtained by interpolating the pressure values p_n and p_{amb}. Further discussion regarding these boundary conditions is provided by Grinstein et al. [13].

The initial conditions required for integrating the particle equations involve the specification of X_p and V_p at a specified initial time. The initial particle velocity is assumed to be the same as that of the slow gas stream. The initial X position for all the particles is the inflow boundary, i.e. $X_p = 0$, whereas the initial y position is varied in a parametric manner depending upon the number of injection locations. For the base case, five injection locations near the centerline in the cross-stream direction are specified. This means that starting at a specified initial time, which is a parameter in the study, five particles are injected with a specified frequency. The dynamics and dispersion behavior of these particles is then computed by numerically solving equations (6) and (7). Note that the solution of these equations is coupled dynamically with that of the gas-phase equations (1)–(4), which are being solved simultaneously.

Numerical procedure

The numerical scheme to solve the two-phase equations is based on a Eulerian–Lagrangian formulation. The algorithm to solve the Eulerian gas-phase equations is based on the Flux Corrected Transport (FCT) methodology. The particle equations are integrated using a second-order Runge–Kutta procedure. The generic algorithm employing the FCT procedure has been tested extensively for large-scale simulations of both nonreacting and reacting flows. It employs a time-step splitting monotone, finite-difference technique. To prevent dispersive errors and maintain positivity, FCT first adds a linear velocity-dependent diffusion to a higher-order approximation during convective transport. The added diffusion is then subtracted out during the antidiffusion stage. The FCT algorithm used was fourth-order phase-accurate. Since the code is based on the solution of a one-dimensional conservation equation, a direction-splitting technique is employed for multidimensional computations. The residual numerical diffusion of the algorithm can effectively emulate physical viscosity for laminar shear flows at moderately high Reynolds numbers [27]. For the (finest) gridding used in this work, the effective viscosity is of the order of air viscosity at STP. Another useful feature of the code is that the variable mesh size can be handled routinely since it employs a control-volume formulation.

Starting at time $t = 0$, the gas-phase equations are integrated to simulate the dynamics of large scale vortical structures. At a specified time during this simulation, the particle injection is started. The trajectories of various particles are tracked by solving equations (6)–(7) by using a second-order Runge–Kutta method. Note that the particle positions in general do not coincide with the fixed gas-phase grid points. A two-dimensional interpolation is employed to calculate the gas-phase properties, such as velocities and density which appear in equations (8)–(9), at the instantaneous particle positions.

RESULTS AND DISCUSSION

Shear layer simulation

First, we describe the results of free shear layer simulation without the particles. These results focus on the transition from a uniform shear flow to a pair of vortices due to the (initial) Kelvin–Helmholtz instability mechanism, followed by subsequent vortex roll-ups due to a feedback mechanism [7, 26], and vortex merging downstream.

The computational domain and the non-uniform grid used in the simulation are shown in Fig. 2. The splitter plate is located upstream of the left boundary at $y = 3.0$ cm. Initially, the two streams are assumed to have the same pressure (1 atm) and temperature (298 K), and uniform velocities V_s and V_f for the slow and fast streams respectively. For the base case, the slower stream is at the top, and the values of V_s and V_f are 20.0 m/s and 100 m/s respectively. As mentioned earlier, two velocity profiles considered at the inflow boundary are the step-velocity and the hyperbolic tangent-velocity profiles. Several test cases were run to establish the grid-independence of results and to study the effect of inflow velocity profiles. The two computational grids used for these tests

employed 200×90, 150×60 and 120×46 grid points respectively. The temporal step sizes used are 5.0×10^{-7} and 2.5×10^{-7} s. For these spatial and temporal step sizes, the results were found to be relatively independent of the step sizes and the inflow velocity profiles. The grid independence was also determined by verifying the scaling of the results with the initial vorticity thickness, Θ [28]. For the results presented here, a temporal step size $= 5.0 \times 10^{-7}$ s and 150×60 grid are employed.

Figure 3 shows a sequence of vorticity contours at $t = 0.9$, 1.06 and 1.22 ms. The corresponding transverse velocity contours are shown in Fig. 4. The pairing and merging of two vortices as they convect downstream, and the formation of a new vortex upstream in the shear layer are clearly illustrated in these figures. The newly formed vortex then pairs with the previously merged vortices. Subsequent merging processes of this kind are responsible for the growth of the shear layer downstream. Another important feature of the mixing-layer development, inherently dependent on its spatially-evolving nature, is the asymmetric entrainment, by which there is more of the high-speed fluid entrained by the large-scale structures as compared to low-speed fluid. This is suggested in Fig. 3 by the gradual shift of the shear-layer center towards the slower side. This asymmetry, observed experimentally by Koochesfahani *et al.* [30] and in the simulations of
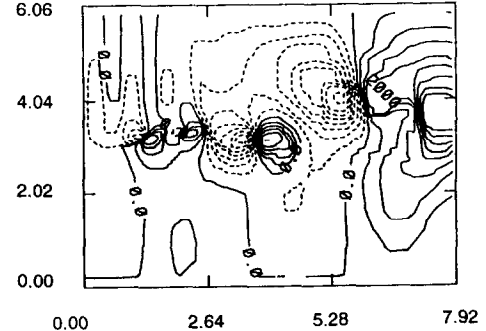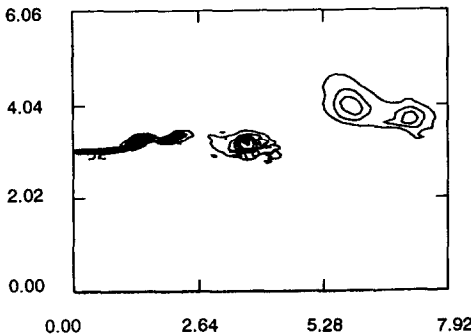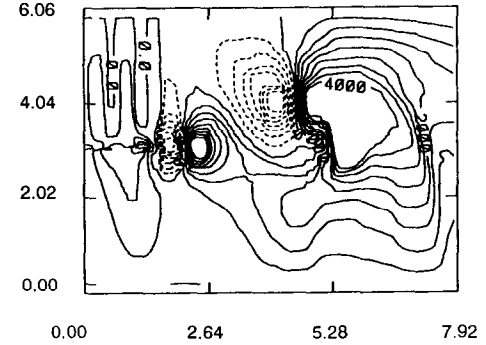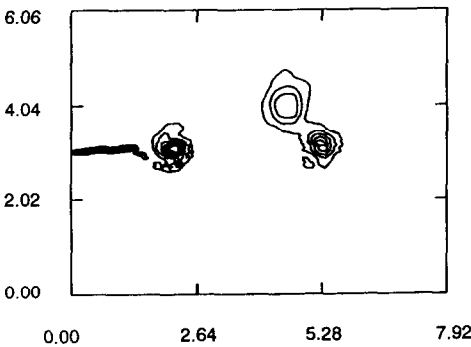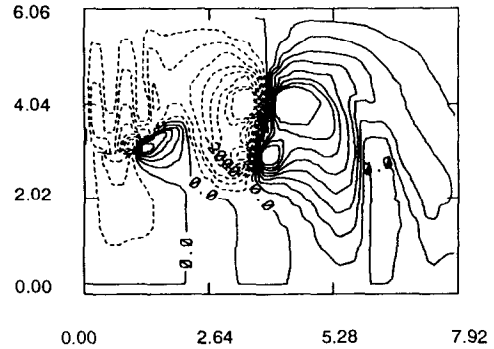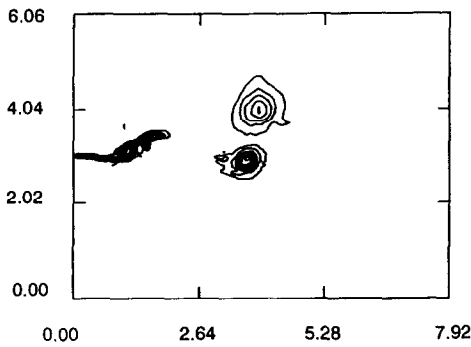

Fig. 3. Sequence of vorticity contours at time $t = 0.9$, 1.06, and 1.22 ms. Contour values range from 7000 to 160,000 s^{-1} with an interval of 9000 s^{-1}.

Fig. 4. Transverse velocity contours at $t = 0.9$, 1.06, and 1.22 ms for the case in Fig. 3. Contour values range from -4000 to 4000 cm/s with an interval of 500 cm/s.
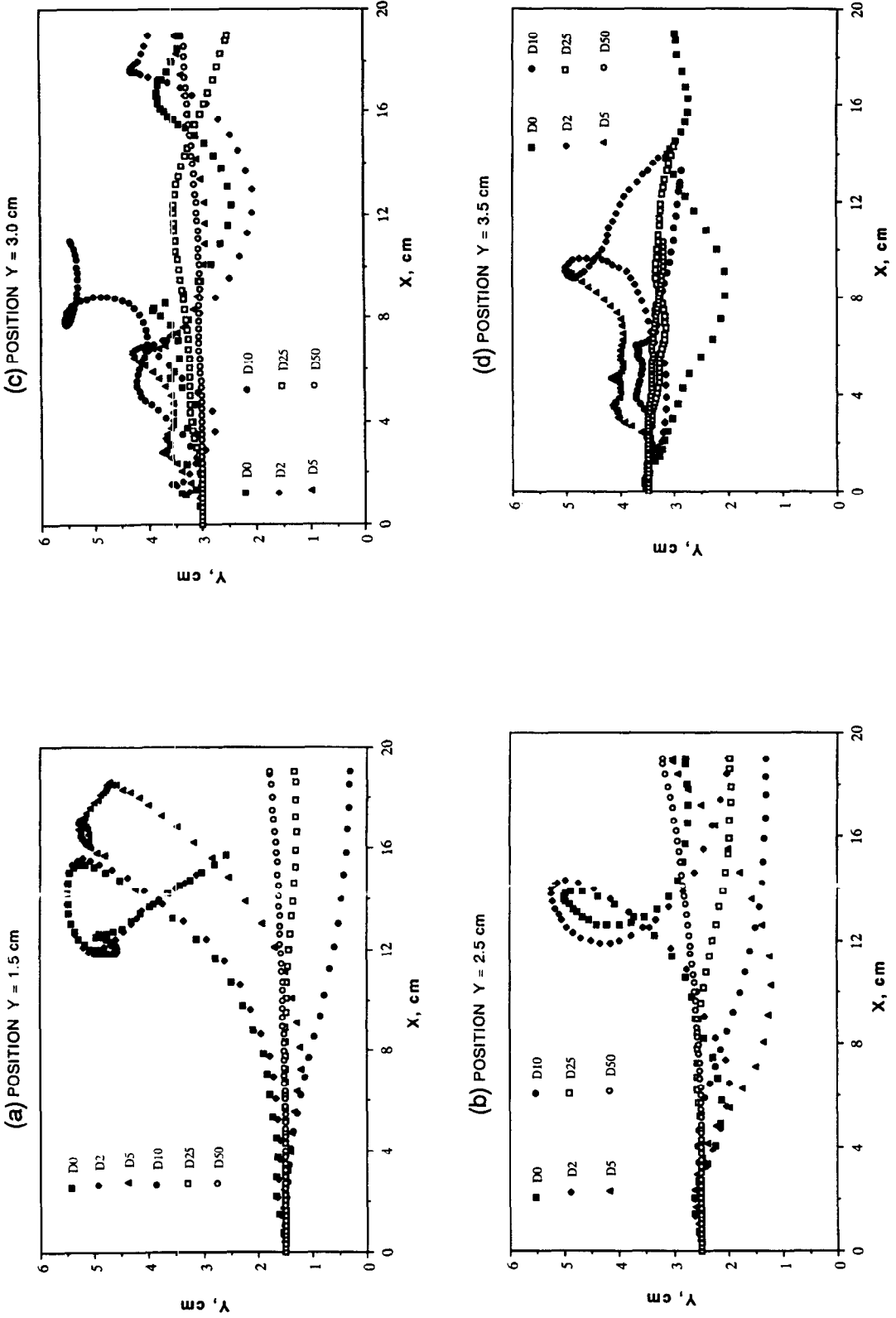
Fig. 5. Trajectories of particles with diameter = 2, 5, 10, 25, and 50 microns. The trajectory of a tracer (gas-phase) particle indicated by Do is also shown. Each figure represents a different injection location. For example, in (a), the particles are injected at $y = 1.5$ cm and so on.

Table 1. Stokes numbers vs particle diameters

d_p (μm)	t_p (ms)	$S_{t1} = t_p/t_{f1}$	$S_{t2} = t_p/t_{f2}$
2	0.012	0.07	4.05
5	0.076	0.45	25.30
10	0.304	1.78	101.25
25	1.897	11.14	632.80
50	7.590	44.55	2531.25

Grinstein *et al.* [13], influences the amount of relative dispersion experienced by the particles discussed later. An elegant discussion of asymmetric entrainment is also given by Dimotakis [29], where the excess entrainment of high-speed fluid is shown to be a result of the geometric progression of successive structures, a feature attributable only to a spatially developing layer.

To obtain the natural instability frequency, the spectral analysis of the axial and transverse velocities recorded at selected spatial locations is performed. The dominant frequency corresponding to the shear layer roll-up or vortex shredding is observed to be 5860 Hz. The corresponding Strouhal number, $S_\Theta = f\,\Theta/U_m$, is 0.024, based on Θ, and the mean velocity, $U_m = 60.0$ m/s. This Strouhal number is in fairly good agreement with the value predicted for the most amplified mode by linear stability theory as well as with experimental measurements [31]. Moreover, in a separate study [32], the roll-up frequency was computed for a number of cases, where the mean velocity (or Reynolds number), velocity ratio, and initial momentum thickness were varied. The Strouhal number for all these cases ranged between 0.023 and 0.027, which is within the experimentally observed range. See, for example, Hussain and Hussain [31] who conducted a comprehensive experimental study of the mixing layer and reported the Strouhal number in the range 0.025–0.031.

Particle dynamics simulations

Figure 5 shows the trajectories of particles that are injected at the inflow boundary and traverse the unsteady flow field dominated by large scale vortical structures. For this case, the shear layer simulation is started at time $t = 0$ and the particles are injected at $t = 2.4$ ms. During this period, $0 < t < 2.4$ ms, the initial flow transient is nearly out of the computational domain and the large-scale structures have assumed a quasi-periodic behavior. The trajectories are computed from $t = 2.4$ to 7.2 ms by solving the gas-phase and the particle equations simultaneously. As indicated in the figure, the particle trajectories are strongly influenced by their size and injection location.
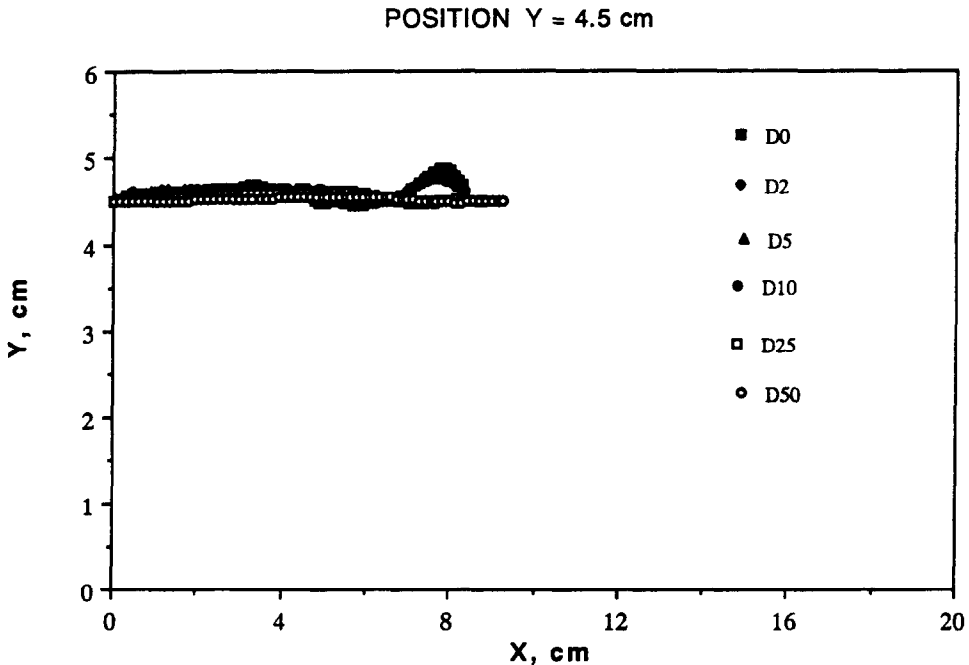
POSITION Y = 4.5 cm

Fig. 6. Trajectories of particles with diameter = 0, 2, 5, 10, 25, and 50 μm injected at $y = 4.5$ cm.

In general, the small particles $(d_p < 5\,\mu\text{m})$ follow the tracer (gas) particles, whereas the large particles $(d_p > 25\,\mu\text{m})$ remain relatively unaffected by the large scale structures as they convect through the shear layer. The intermediate size particles $(d_p = 10\,\mu\text{m})$ exhibit very interesting behavior. Their trajectory, although completely different from that of the tracer particles, is strongly influenced by the larger-scale structures. In fact, depending upon the injection location, their trajectories are influenced even more strongly by the large-scale structures compared to that of tracer particles, i.e. they are dispersed more than the gas particles. This is clearly the case for $10\,\mu\text{m}$ particles injected at the tip of the splitter plate $(y = 3.0\,\text{cm})$. As shown in Fig. 5(c), the dispersion of $10\,\mu\text{m}$ particle is significantly greater than that of gas particle. As discussed by Yule [33] and Crowe *et al.* [10], the intermediate size particles are entrapped by the large eddies and then dispersed into the potential flow due to the centrifugal action. On the other hand, the smaller particles remain trapped in the eddies. Thus, the present results provide further evidence that the intermediate size particles can disperse significantly more than the gas particles. The relative
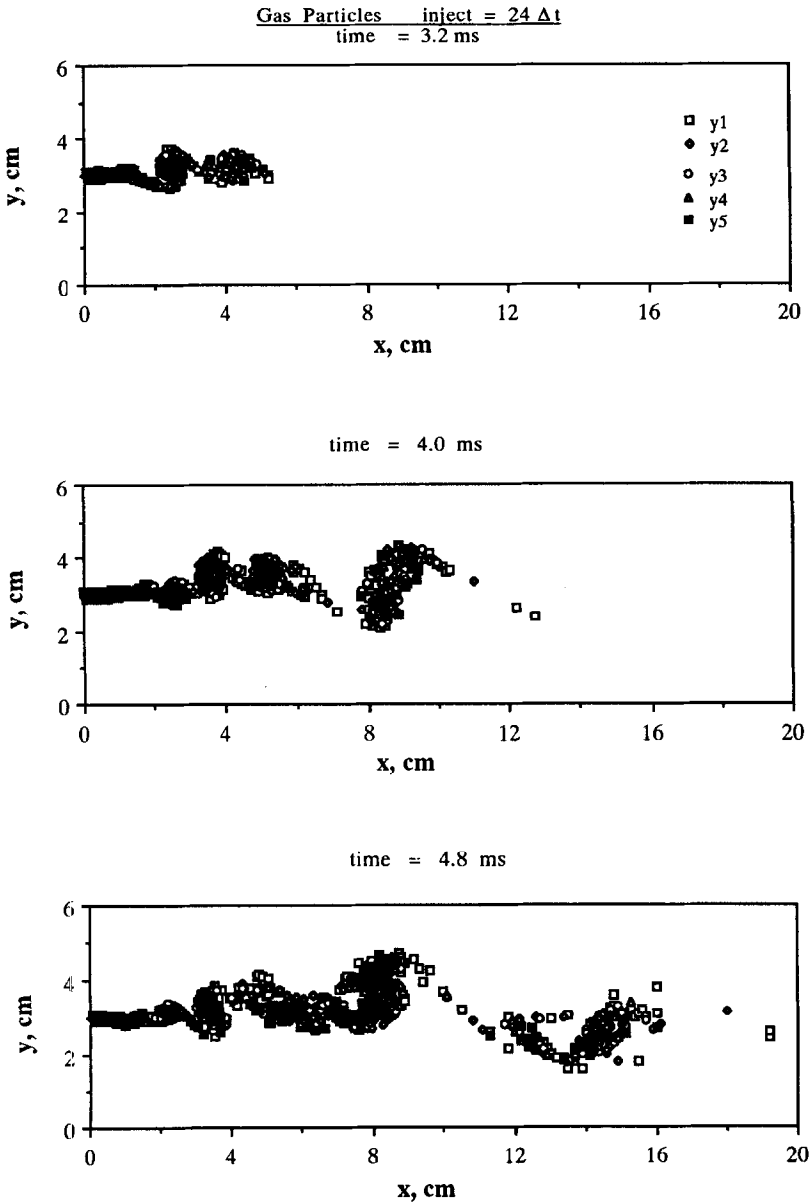

Fig. 7. Snapshots of gas particle $(d_p = 0)$ positions at $t = 3.2$, 4.0, and 4.8 ms. The injection is started at 2.4 ms and five particles are introduced at the left boundary after every 0.012 ms. The injection location are $y_1 = 2.9$, $y_2 = 2.95$, $y_3 = 3.0$, $y_4 = 3.05$, and $y_3 = 3.1$ cm.
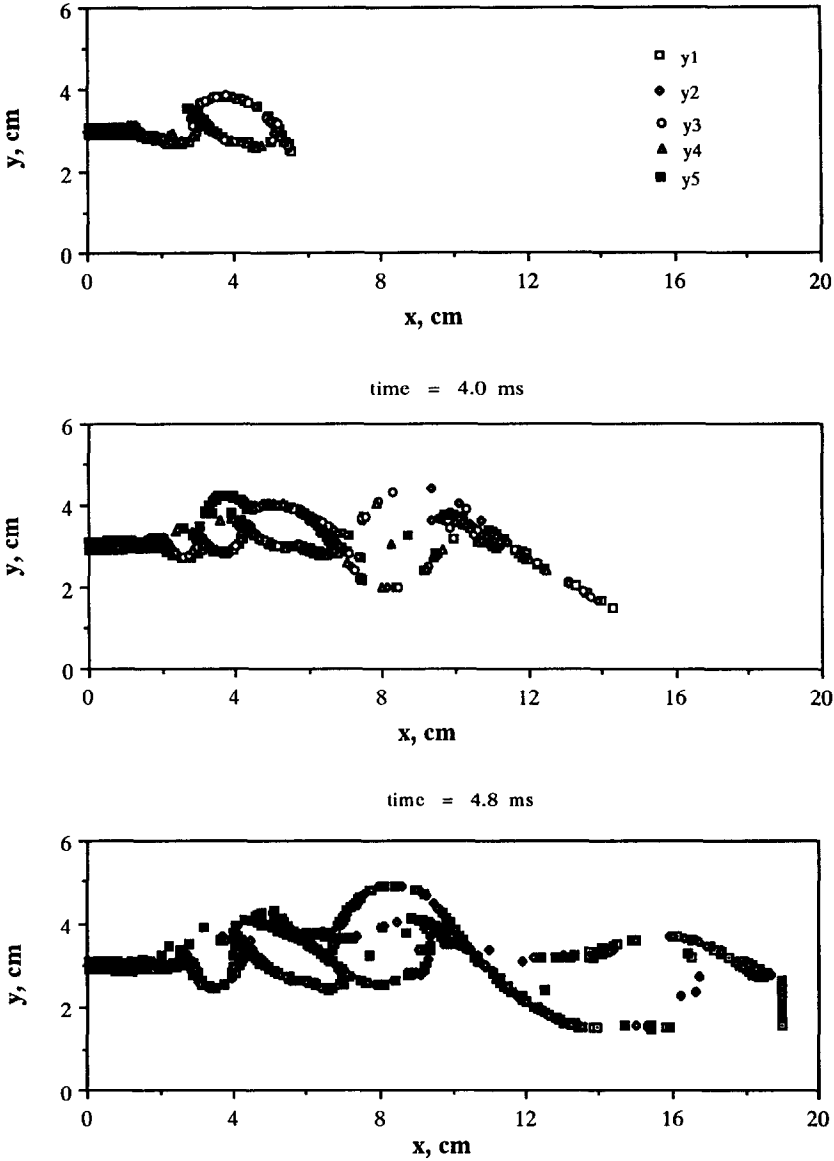
Fig. 8. Snapshots of particle positions at $t = 3.2$, 4.0, and 4.8 ms. The particle diameter $d_p = 5\,\mu$m. The Stokes number $S_t = 0.45$. Other parameters are the same as in Fig. 7.

amount of dispersion, however, depends strongly on the location from where the particles are injected. This aspect is discussed further in the next section where the dispersion effect is quantified.

Let us now represent the increased dispersion for the intermediate size particles in terms of the Stokes number, defined as the ratio of the particle response time to the characteristic flow time, i.e.

$$S_t = t_p/t_f. \tag{12}$$

The particle response time is generally defined [21] as

$$t_p = \frac{\rho_p d_p^2}{18\mu} \tag{13}$$

where μ is the viscosity of the continuous phase. Note that this definition is based on the Stokes drag law [24] and would overpredict the particle response time in realistic situations. For example,

if equation (9) is employed for calculating the drag coefficient, it would yield a smaller value of t_p. We will, however, use equation (13) for computing the Stokes number, since this is the accepted definition in literature. The particle response time as a function of the particle diameter is given in Table 1. The characteristic flow time in equation (12) may be defined in two different ways. One is to use the natural instability or the roll-up frequency defined earlier in terms of the Strouhal number S_Θ, which gives

$$t_\text{fl} = \frac{\theta}{S_\theta U_\text{m}} \tag{14}$$

where

$$U_\text{m} = \frac{V_\text{f} + V_\text{s}}{2}.$$
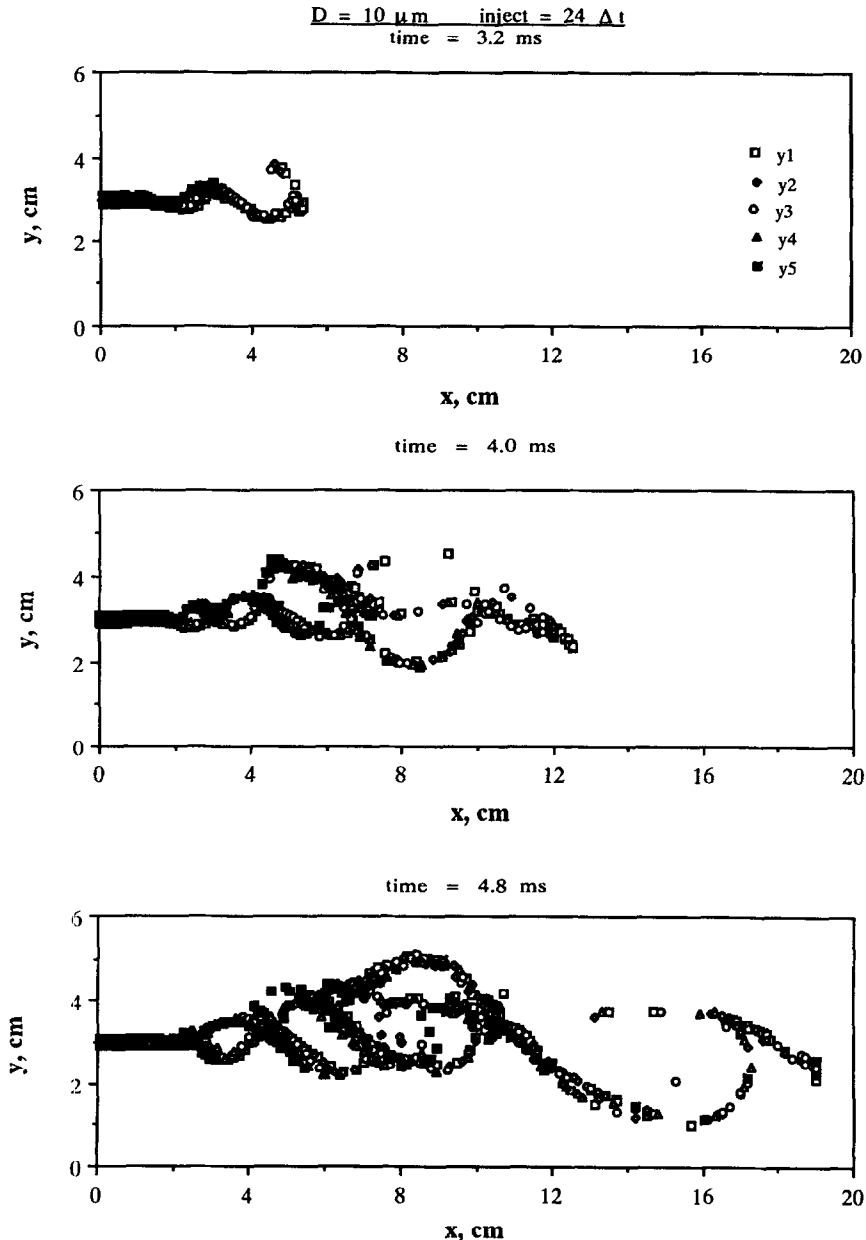
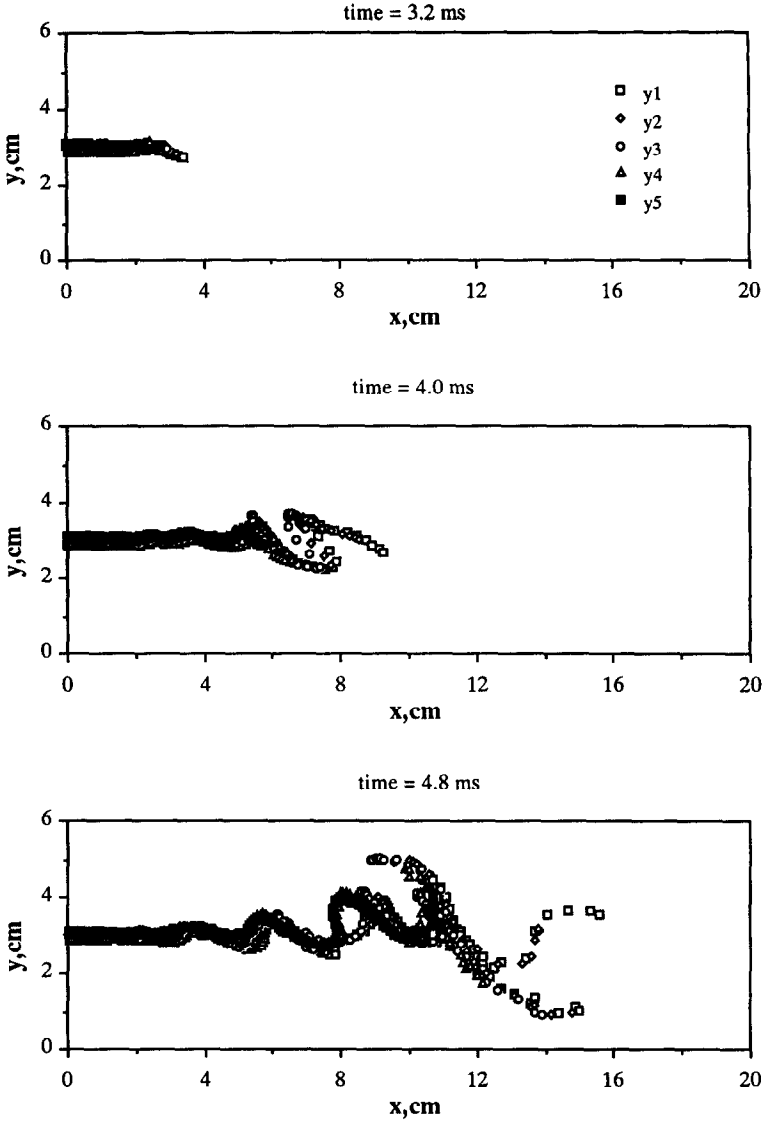Fig. 9. Snapshots of particle positions at $t = 3.2$, 4.0, and 4.8 ms. $d_\text{p} = 10\,\mu\text{m}$, $S_t = 1.78$.

Fig. 10. Snapshots of particle positions at $t = 3.2$, 4.0, and 4.8 ms. $d_p = 20\,\mu$m, $S_t = 7.12$.

The other way is to employ the initial strain rate, defined as $(V_f - V_s)/\Theta$, where Θ is the smallest grid size in the transverse direction. This gives

$$t_{f2} = \frac{\theta}{V_f - V_s}. \tag{15}$$

For the particle sizes considered, we have calculated the Stokes number using both the characteristic flow times. The results are summarized in Table 1. There are two important observations from the table. First, the correct time scale to be used for calculating the Stokes number should be based on the natural instability frequency, and not the initial (maximum) strain rate. Perhaps, the appropriate length scale for defining the strain rate in equation (15) should be the characteristic size (λ) of the large scale structures. Then, by replacing Θ by λ and equating equations (14) and (15), one obtains

$$\frac{\lambda}{\theta} = \frac{V_f - V_s}{f\theta} \tag{16}$$

which states that the large eddy size can be represented in terms of the initial strain rate and the natural instability frequency. Using the values for the base case, the non-dimensional eddy size $\lambda/\Theta = 56.9$, yielding $\lambda = 1.37$ cm, which agrees with the value estimated from the vorticity contour plots.

The second important observation is the remarkable degree of correlation between the enhanced particle dispersion and the values of the Stokes number in the range $0.1 < S_t < 5$. For example, for the $10\,\mu$m particle, the value of the Stokes number is 1.78. For $S_t < 0.1$, the particles closely follow the large scale vortical structures, as shown in Fig. 5. For $S_t > 5.0$, corresponding to $d_p = 25$ and $50\,\mu$m, the particles are relatively unaffected by the large scale structures. This observation is consistent with the results of Chein and Chung [22]. Note, however, that in the present study, the time scale of the large scale structures is calculated from the roll-up frequency obtained numerically, whereas in the cited reference, it is based on the width of the mixing layer. In addition, the present results indicate the asymmetric nature of the dispersion enhancement phenomenon. The intermediate size particles ($0.1 < S_t < 5.0$) injected into the fast stream ($y < 3.0$ cm) exhibit a greater degree
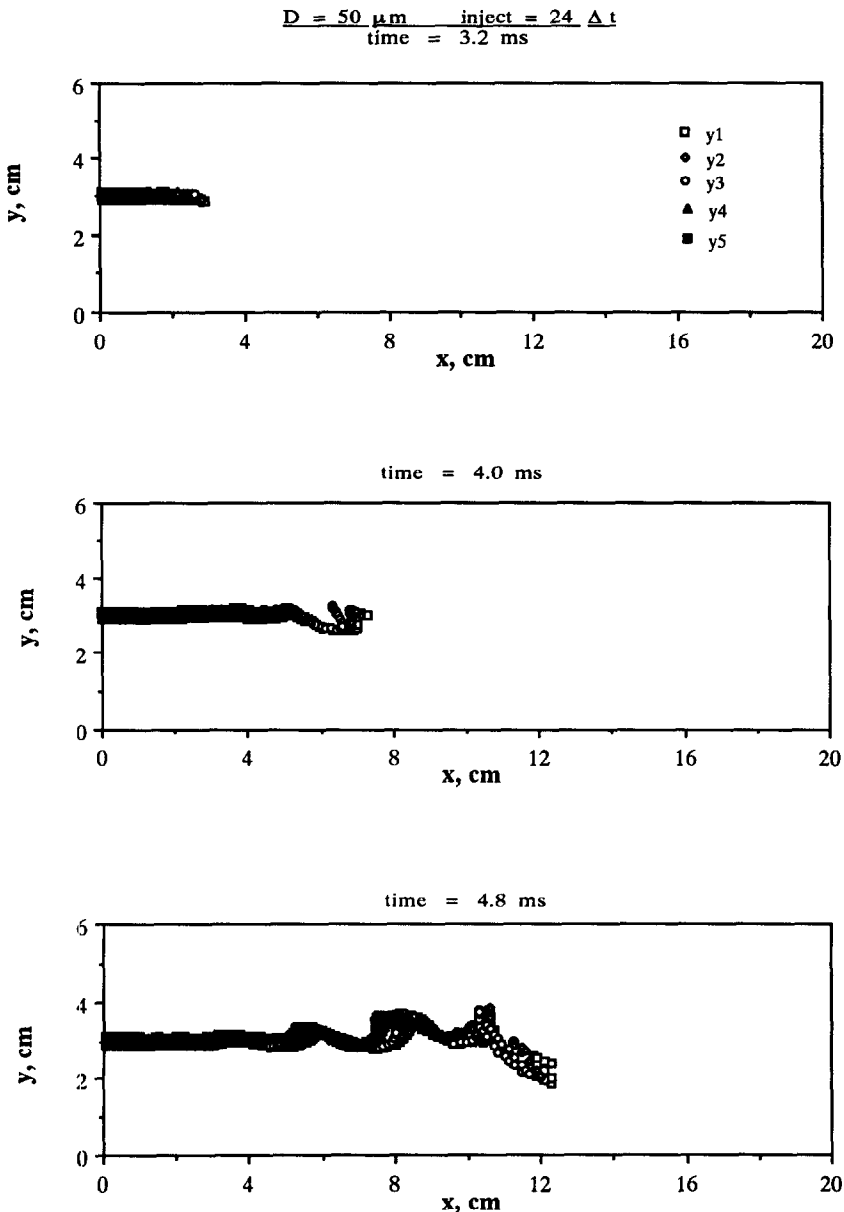

Fig. 11. Snapshots of particle positions at $t = 3.2$, 4.0, and 4.8 ms. $d_p = 50\,\mu$m, $S_t = 44.55$.

of dispersion compared to those injected into the slow stream ($y < 3.0$ cm). This is clearly indicated by the comparison of particle trajectories in Figs 5(a) and 6. The particles injected from $y = 1.5$ cm [Fig. 5(a)] are dispersed much more than those injected from $y = 4.5$ cm (Fig. 6), although the injection location relative to the splitter plate ($y = 3.0$ cm) is the same for both cases. The difference in the degree of dispersion is related to the asymmetry of the entrainment process discussed earlier.

Let us summarize the important observations emerging from the results presented so far. First, the effect of large vortical structure is to enhance significantly the dispersion of intermediate size particles. The degree of enhancement, however, depends upon the transverse injection location
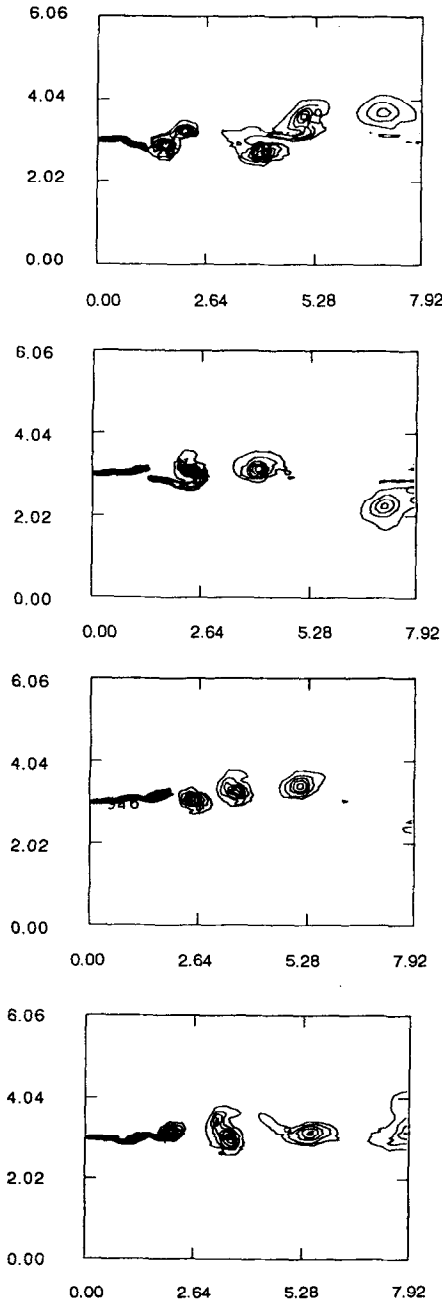

Fig. 12. Vorticity contours at $t = 2.4$, 3.2, 4.0, and 4.8 ms. Contour values range from 7000 to 160,000 s^{-1} with an interval of 9000 s^{-1}. The slow and fast stream (see Fig. 1) velocities are 20.0 and 100.0 m/s respectively.
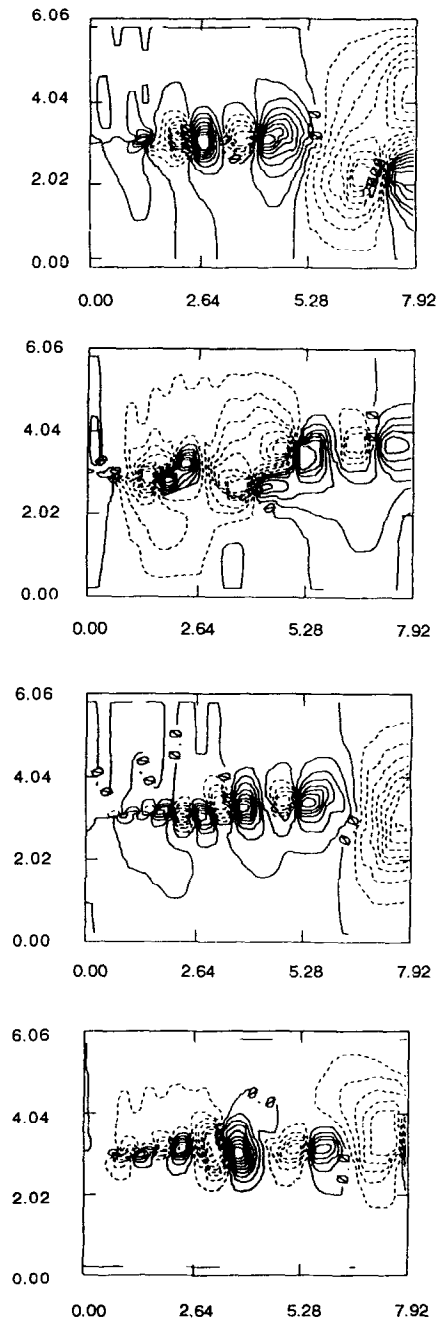
Fig. 13. Transverse velocity contours for the case shown in Fig. 13. The contour values are -4000 to 4000 cm/s with an interval of 500 cm/s.
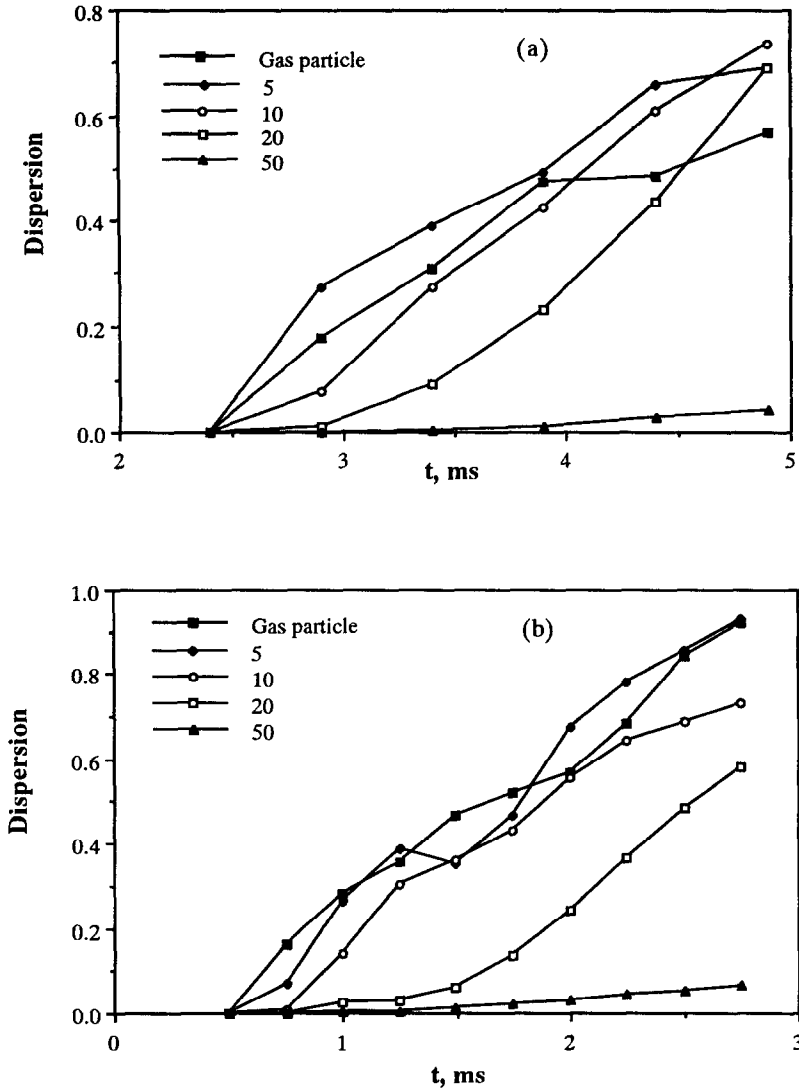
Fig. 14. Variation of particle dispersion function with time t for an established as well as a developing shear layer. Particle sizes are 0 (gas particles), 5, 10, 20, and 50 μm. (a) Particles injected for period $2.4 < t < 4.8$ ms; (b) particles injected for period $0.5 < t < 2.9$ ms.

relative to the splitter plate. Not only is the distance from the splitter plate important, but also from which side of the plate, the particles are injected, plays a significant role in the relative enhancement of dispersion. The particles injected on the high-speed side are dispersed more compared to these injected on the low-speed side. This is due to the asymmetry of the mixing process as discussed earlier. Second, the enhanced dispersion for the intermediate size particles can be correlated to the Stokes number range $0.1 < S_t < 5$. It is important to note, however, that the calculation of the Stokes number is based on the natural instability frequency of the shear layer.

Particle dispersion results

In order to quantify the particle dispersion behavior, a continuous injection of particles from the upstream boundary is simulated. Again the flow computation is started at $t = 0$, and the particle injection is started at 2.4 ms. As mentioned earlier, by this time, the initial transient is out of the computational domain and the flow field is nearly developed. The time interval between two consecutive injections is 0.012 ms, i.e. starting at $t = 2.4$ ms, a fixed number of particles are injected into the flow field after every 0.012 ms. Note that the characteristic flow time obtained from the natural instability frequency is 0.171 ms, which corresponds to 14 injections.

The results of this simulation from $t = 2.4$ to 4.8 ms are portrayed in Figs 7–11. In order to understand these results better, the unsteady shear layer development is shown in Figs 12 and 13, where the vorticity and transverse velocity contours are plotted at different times. For the results shown in Figs 7–11, the particles are injected from five transverse locations; $y = 2.9$, 2.95, 3.0, 3.05, and 3.10 cm. Figure 7 shows the snapshots of gas particle ($d_p = 0$) positions at three different times, $t = 3.2$, 4.0, and 4.8 ms respectively. For $d_p = 0$, these snapshots are more commonly referred to as the streamlines. The corresponding results for particles of diameter of 5, 10, 20, and 50 μm are given in Figs 8–11. The Stokes numbers corresponding to these diameters are 0.45, 1.78, 7.12 and 44.55 respectively. Note that at $t = 4.8$ ms, there are 1000 particles in the flow field for each case.

The streaklines for gas particles at $t = 4.8$ ms in Fig. 7 further show the growth of the shear layer due to the processes of vortex roll-up and merging. These processes can also be visualized by the vorticity contours in Fig. 12, and the transverse velocity contours plots in Fig. 13. A more important observation is the greater amount of dispersion exhibited by the intermediate size particles ($S_t = 0.45$ and 1.78) compared to that by the gas particles. This can be clearly seen by comparing Figs 8 and 9, which correspond to $S_t = 0.45$ and 1.78 respectively, with Fig. 7. For high

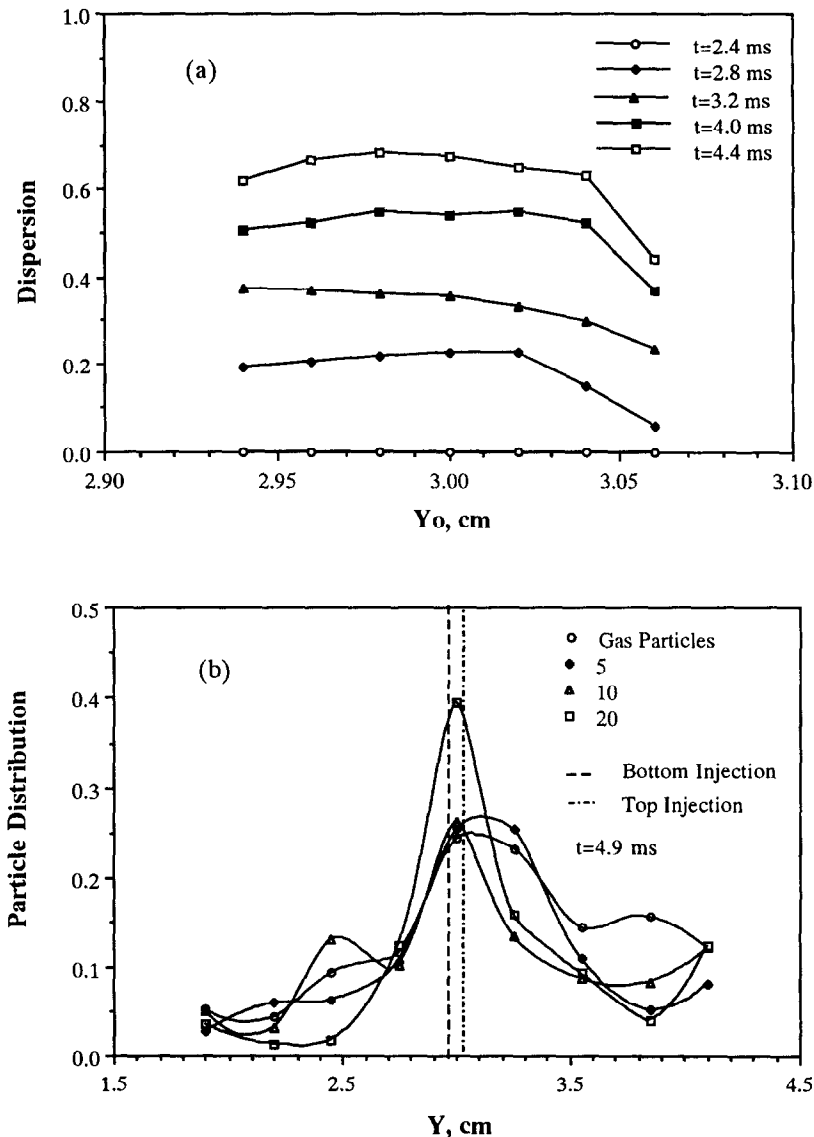

Fig. 15. (a) Variation of dispersion function with the initial injection location. Particle diameter = 5 μm; (b) normalized particle distribution plotted versus the cross stream locations for $d_p = 0$, 5, 10, and 20 μm.
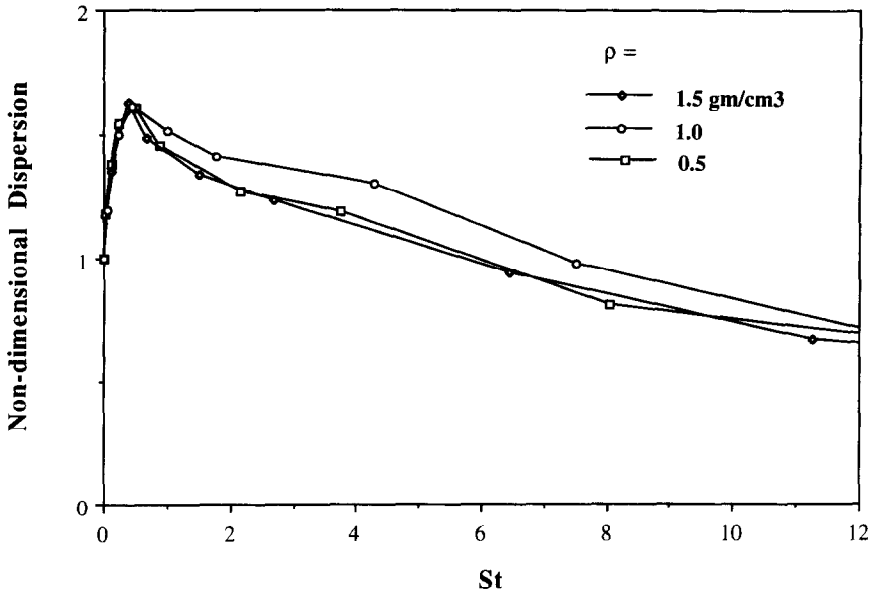
Fig. 16. Dispersion function plotted versus Stokes number for different particle densities.

Stokes numbers, $S_t = 49.28$, the amount of dispersion (see Figs 10 and 11) is small compared to that of the gas particles. In order to quantify the amount of dispersion, the dispersion function [23] is defined as

$$D(t, N) = \left(\sum_{i=1}^{N} (y_i(t) - y_{io})^2/N \right)^{1/2}$$

where N is the total number of particles in the flowfield at time t, y_i the transverse location of particle i at time t, and y_{io} the transverse location of the same particle at the inflow boundary. It can be expected that the dispersion function is a strong function of t and the particle diameter d_p. In addition, it may be a function of the initial particle location, y_{io}, the total number of particle N, and the time when the injection is started. Figure 14 shows the variation of the dispersion function with time in an established shear layer for various particle sizes. The Stokes numbers for

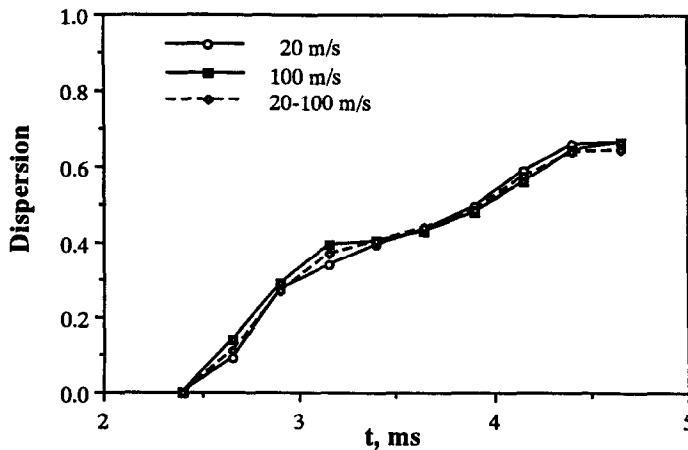Fig. 17. Dispersion function plotted versus time for different initial particle velocities for 5.0 μm particles. Case 1: particles injected at 20.0 m/s, Case 2: particles injected at 100.0 m/s, Case 3: particles injected at the local gas velocity.

the sizes considered are 0, 0.45, 1.78, 7.12, and 44.45 corresponding to the diameters 0, 15, 10, 20, and 50 μm. The important observations are as follows:

(i) The dispersion function generally increases with time since the particles disperse increasing farther from their injection location. For smaller particles, the variation is somewhat irregular indicating the greater influence of the large scale structures on particles. As the particle size increases, the variation of $D(y, t)$ becomes more regular.

(ii) The variation of $D(y, t)$ with the particle size clearly demonstrates the enhancement of particle dispersion in the intermediate size range. At earlier times, the dispersion seems to be the highest for the 5 μm particles ($S_t = 0.45$). At later times, however, the 10 μm particles ($S_t = 1.78$) exhibit the highest amount of dispersion.

(iii) The quantitative results presented in Fig. 14 are consistent with the qualitative results given in Fig. 5 and Figs 7–11. They are also in agreement qualitatively with the results of Chung and Troutt [23] on the dispersion of particles in an axisymmetric jet.

(iv) Another important parameter influencing the dispersion function is the instant at which the particle injection is started. The dependence of the dispersion function on the particle size
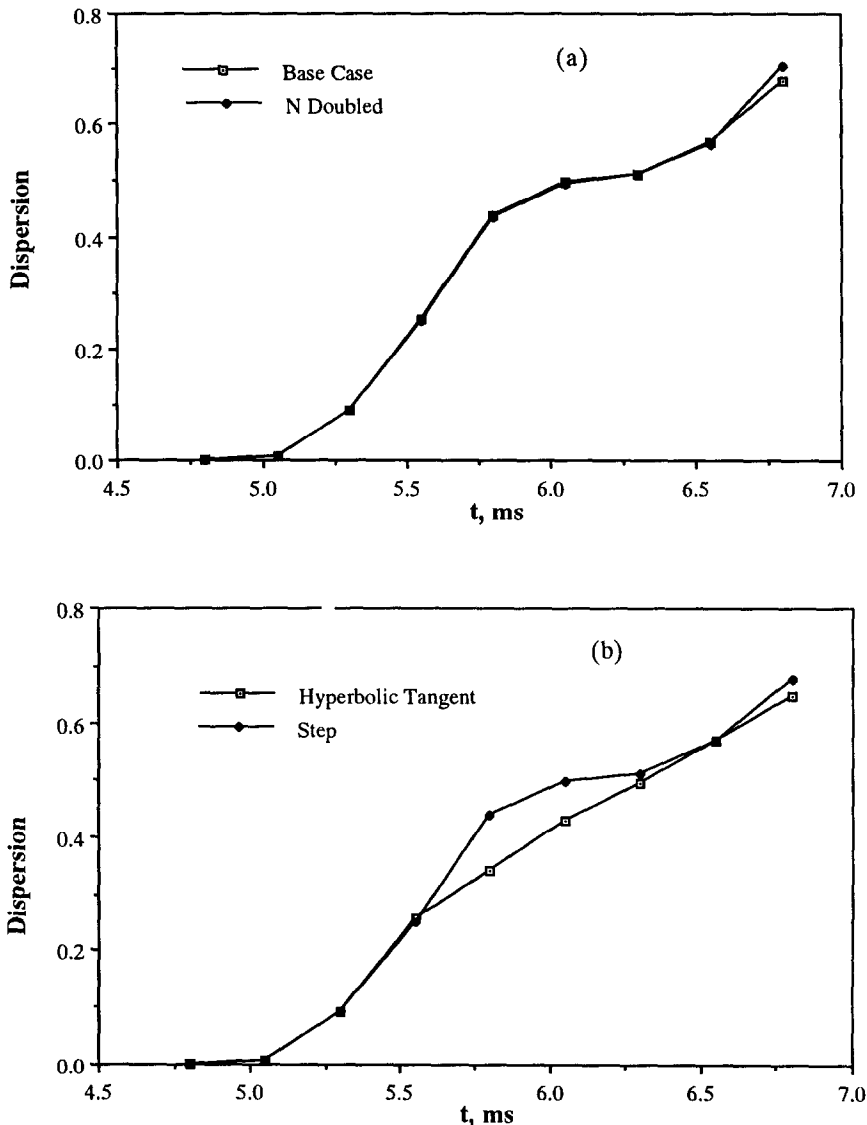

Fig. 18. Effect of the total number of particles (a) and the inflow gas velocity profiles (b) on the particle dispersion. The particle diameter = 5.0 μm.

changes significantly, if the particles are injected during the early shear layer development. As shown in Fig. 14(b), the dispersion function does not seem to maximize for the intermediate values of the Stokes number, which is in complete contrast with the more developed shear layer case [Fig. 14(a)].

(v) As indicated in Fig. 15(a), the dispersion function also varies with the particle injection location. The particles injected in the fast stream ($y_{io} < 3.0$ at time $t = 0$) disperse more compared to those injected in the slow stream ($y_{io} > 3.0$). This difference in dispersion is related to the asymmetry of the entrainment process discussed earlier. The asymmetric dispersion behavior can also be demonstrated by plotting the normalized particle distribution (P_n) as a function of the cross stream location, shown in Fig. 15(b). Here P_n is defined as the probability of having a particle in a given cross stream region. Note that all the particles are injected from cross stream locations between $2.96 < Y_o < 3.04$ cm, the region marked by two broken lines in Fig. 15(b). Without dispersion, all the particles would be confined to this region, and P_n will maintain a value of 1.0 there and zero outside. Due to dispersion, however, the distribution curve would become broader with a lower peak. The important observation is that the distribution curve is asymmetric, indicating more particles on the slow stream side ($Y > 3.0$ cm) compared to the fast stream side.

In order to quantify the effect of particle size on dispersion, the dispersion function is plotted versus Stokes number for three different particle densities. For this plot shown in Fig. 16, the dispersion function is averaged both spatially and temporally over all the particles injected from a fixed location. Important observations are that the particle dispersion exhibits a maximum near $S_t = 0.5$ and that the use of initial instability frequency provides the expected correlation between dispersion function and Stokes number. The results presented so far are for particles injected with the local gas velocity of slow stream. The effect of particle injection velocity on dispersion is portrayed in Fig. 17, where the dispersion function for the $5.0\,\mu$m particles is plotted for three different cases. The figure clearly indicates that, for the configuration considered, the particle injection velocity does not influence the dispersion behavior significantly. In this context, it is interesting to mention the more recent work of Wang [34], where it is shown that the dispersion behavior can be altered by nonuniform injection of particles. However, the nonuniformity is introduced by controlling the particle number density, and, therefore, represents a different situation compared to that considered here. Another important result is shown in Fig. 18. The effect of the total number of particles on the particle dispersion function, given in Fig. 18(a), clearly indicates that the number of particles considered in obtaining the particle dispersion function is sufficient. For the two cases shown in Fig. 18(a), there are 1000 and 2000 particles respectively. The effect of the inflow gas velocity profiles on dispersion shown in Fig. 18(b) indicates that the numerical results are relatively insensitive to the two velocity profiles considered. This implies that the dynamics of large scale vortical structures and of particles is relatively independent of the two velocity profiles considered.

CONCLUSION

In this study, the numerical simulations of particle dynamics and dispersion in the initial development of the planar shear layer are reported. The shear layer which is formed by two coflowing streams downstream of a splitter plate is simulated by solving the time-dependent inviscid compressible conservation equations. The numerical algorithm is based on the explicit flux corrected transport procedure. A Lagrangian approach is employed to study the particle dynamics and dispersion in the large-scale vortical structures. An extensive visualization of the flow field, dominated by the large structures, and of the particle trajectories is performed to obtain both qualitative and quantitative information on the particle dispersion behavior.

The first part of the simulation focuses on the temporal and spatial growth of the shear layer. As expected, the results on the generation of vorticity clumps due to the Kelvin–Helmholtz instability, and on the growth of shear layer due to vortex pairing agree with those of Grinstein et al. [13]. The spectral analysis of the pressure and velocity histories at selected spatial locations in the shear layer is used to obtain the natural instability frequency and its subharmonics.

The results of the particle dynamics simulations indicate that both small and moderate size particles ($0 < d_p < 20 \, \mu$m) are captured in the vortical structures. While the small size particles, $d_p \leqslant 2 \, \mu$m, remain captured in these structures, the moderate size particles may be flung out of them, causing these particles to disperse more than the tracer (gas) particles. The larger particles remain relatively unaffected by the large structures. The quantitative results, presented in terms of a dispersion function $D(y, t)$ as a function of time and the Stokes number, substantiates these observations. The optimal dispersion is achieved when the Stokes number is in the range $0.1 < S_t < 5.0$. These results are in qualitative agreement with the experimental as well as numerical results reported previously. Another important observation is the dependence of the dispersion function on the transverse injection location. The particles injected in the fast stream disperse more than those injected in the slow stream. This behavior is attributable to the asymmetry of the entrainment process observed here as well as in the experiments of Koochesfahani *et al.* [30] and the simulations of Grinstein *et al.* [13].

As a final note, it is important to mention that the present results compare favorably with those of laboratory experiments in many respects. This includes the Strouhal number for the roll-up frequency (the predicted Strouhal number of a number of cases is in the range 0.023–0.027, whereas the experimental range reported [31] is 0.025–0.031) and the asymmetric entrainment in the shear layer [29]. In addition, the present simulations show greater dispersion for the intermediate size particle as well as for particles injected in the high-speed fluid. Both of these features have also been observed in the experimental study of Lazaro and Lasheras [14, 15], except that in the cited study, the greater dispersion for the intermediate size particles was noted for the forced shear layer. The general result regarding the greater dispersion of intermediate size particles is also reported in several earlier experimental studies, reviewed by Crowe *et al.* [10], and in recent studies by Lazaro and Lasheras [14, 15] and Hishida *et al.* [21]. In particular, the predicted Stokes number for the maximum dispersion in our study is 0.49. This is in agreement with the experimental results of Lazaro and Lasheras [14, 15] that yield a droplet size range 21–35 μm or a Stokes number range 0.18–0.5 for the maximum dispersion. Hishida *et al.* [21] observed enhanced dispersion for 42.0 μm glass particles, yielding a Stokes number of 1.28, based on the dominant frequency reported in their experiments. However, the smallest particle size considered in the experimental study [21] was 42 μm; it is conceivable that the maximum dispersion could have occurred at a lower Stokes number. The present results are also in agreement with the previous numerical predictions on particle dispersion. In particular, Chein and Chung [22] observed the existence of an intermediate particle size range for which the dispersion is maximized. The features that distinguish the present work from that cited above are as follows: (i) the large eddy simulation in the present study is based on the finite-difference flux-corrected transport algorithm, whereas the cited work has employed a discrete vortex method; (ii) a consequence of this difference is the asymmetric particle dispersion observed in the present results, but not captured in the discrete vortex approach; and (iii) a correlation is provided between the Stokes number and the shear layer roll-up frequency. To our knowledge, the last two features have not been reported by previous studies.

REFERENCES

1. J. T. Jurewicz and D. E. Stock, A numerical model for turbulent diffusion in gas–particle flows. ASME WAM Paper No. 76-WA/FE-33 (1976).
2. P. J. Smith, T. J. Fletcher and L. D. Smoot, Model for pulverized coal-fired reactors, *Eighteenth (Int). Symp. on Combustion*, Pittsburgh, PA, pp. 1285–1293 (1981).
3. A. D. Gosman and E. Ioannidees, Aspects of computer simulation of liquid fueled combustors, AIAA-81-0323. *19th Aerospace Sciences Meeting*, St. Louis, Jan. 12–15 (1981).
4. J.-S. Shuen, A. S. P. Solomon, Q.-F. Zhang and G. M. Faeth, Structure of particle laden jets: measurements and predictions. *AIAA J.* **23**, 396 (1985).
5. G. L. Brown and A. Roshko, On density effects and large structures in turbulent mixing layers. *J. Fluid Mech.* **64**, 775 (1974).
6. C. D. Winant and F. K. Browand. Vortex pairing: the mechanism of turbulent mixing layer growth at moderate Reynolds number. *J. Fluid Mech.* **63**, 237 (1974).

7. P. E. Dimotakis and G. L. Brown, The mixing layer at high Reynolds number: large structure dynamics and entrainment. *J. Fluid Mech.* **78,** 535 (1976).
8. C. M. Ho and P. Huerre, Perturbed free shear layers. *Ann. Rev. Fluid Mech.* **16,** 365 (1984).
9. G. M. Corcos and F. S. Sherman, The mixing layer: deterministic models of a turbulent flow. Part 1. Introduction and the two-dimensional flow. *J. Fluid Mech.* **139,** 29 (1984).
10. C. T. Crowe, J. N. Chung and T. R. Troutt, Particle mixing in free shear flows. *Prog. Energy Combust. Sci.* **14,** 171 (1988).
11. B. J. Lazaro and J. C. Lasheras, Particle dispersion in a turbulent, plane, free shear layer. *Phys. Fluids A* **1(6),** 1035 (1989).
12. J. P. Boris and D. L. Book, Solution of continuity equation by the method of flux corrected transport. In *Methods in Computational Physics* **16,** 85 (1976).
13. F. E. Grinstein, E. S. Oran and J. P. Boris, Numerical simulation of an asymmetric mixing in planar shear flows. *J. Fluid Mech.* **165,** 201 (1986).
14. B. J. Lazaro and J. C. Lasheras, Particle dispersion in the developing free shear layer. Part 1. Unforced flow. *J. Fluid Mech.* **235,** 143 (1992).
15. B. J. Lazaro and J. C. Lasheras, Particle dispersion in the developing free layer. Part 2. Forced flow. *J. Fluid Mech.* **235,** 179 (1992).
16. J. J. Riley and R. W. Metcalfe, Direct numerical simulation of a perturbed turbulent mixing layer. AIAA Paper 80-0274 (1980).
17. K. Z. Korczak and R. A. Wessel, Mixing control in a plane shear layer. *AIAA J.* **27,** 1744 (1989).
18. A. F. Ghoniem and K. K. Ng, Numerical study of the dynamics of a forced shear layer. *Phys. Fluids* **30,** 706 (1987).
19. F. F. Grinstein, F. Hussain and E. S. Oran, Vortex-ring dynamics in a transitional subsonic free jet. A numerical study. *Eur. J. Mech., B/Fluids* **9,** 499 (1990).
20. R. W. Davis and E. F. Moore, A numerical study of vortex merging in mixing layers. *Phys. Fluids* **28,** 1626 (1985).
21. K. Hishida, A. Ando and M. Maeda, Experiments on particle dispersion in a turbulent mixing layer. *Int. J. Multiphase Flow* **18,** 181 (1992).
22. R. Chein and J. N. Chung, Effects of vortex pairing on particle dispersion in turbulent shear flows. *Int. J. Multiphase Flow* **13,** 785 (1987).
23. J. N. Chung and T. R. Trout, Simulation of particle dispersion in an axisymmetric jet. *J. Fluid Mech.* **186,** 199 (1988).
24. R. Clift, J. R. Grace and M. E. Weber, *Bubbles, Drops, and Particles.* Academic, New York (1978).
25. G. M. Faeth, Mixing, transport and combustion in sprays. *Prog. Energy Combust. Sci.* **13,** 293 (1987).
26. F. F. Grinstein, E. S. Oran and J. P. Boris, Pressure field, feedback and global instabilities of subsonic spatially developing mixing layers. *Phys. Fluids A* **3,** 2401 (1991).
27. F. F. Grinstein and R. H. Guirguis, Effective viscosity in the simulation of spatially evolving shear flows with monotonic FCT models. NRL Memorandum Report #6926 (1991); *J. Comp. Phys.* **101,** 165 (1992).
28. L. Kung, Numerical simulations of unforced and forced shear layers. M.S. Thesis, Department of Mechanical Engineering, The University of Illinois at Chicago (1992).
29. P. E. Dimotakis, Two-dimensional shear-layer entrainment. *AIAA J.* **24,** 1791 (1986).
30. M. M. Koochesfahani, P. E. Dimotakis and J. E. Broadwell, A flip experiment in a chemically reacting turbulent mixing layer. *AIAA J.* **23,** 1191 (1985).
31. Z. D. Hussain and A. K. M. F. Hussain, Natural instability of free shear layers. *AIAA J.* **21,** 1512 (1983).
32. L. Kung and S. K. Aggarwal, Simulation of unforced and forced shear layers. *Int. J. Comput. Fluid Dyn.*, submitted.
33. A. J. Yule, Investigation of eddy coherence in jet flows. In *The Role of Coherent Structures in Modeling Turbulence and Mixing, Proc. Int. Conf.* (Edited by J. Jimenez), pp. 188–207. Springer, Berlin (1980).
34. L. P. Wang, Dispersion of particle injected nonuniformly in a mixing layer. *Phys. Fluid A* **4,** 1599 (1992).